

Chapter 16. Atmospheric Vortex Streets and Gravity Waves

Xiaofeng Li

Office of Research and Applications, NOAA/NESDIS, Camp Springs, Maryland, USA

16.1 Introduction

Under favorable conditions, when stratified air flows around an obstacle such as a mountain or an island, atmospheric vortex streets (AVS) or atmospheric gravity waves (AGW) often develop around the obstacle. The AVS consists of counter rotating vortex-pairs shedding alternately near each edge of the obstacle and resembles the classic Von Kármán vortex-street patterns (Figure 16.1). AGW generated by flow over topography can happen on either side of an obstacle. An AGW on the lee side of a mountain or an island is called a lee wave. Lee waves have two types of wave patterns: (1) the transverse wave type where the wave crests are nearly perpendicular to the wind direction; and (2) the diverging wave type where the wave crests are orientated outwards from the center of the wake. Laboratory experiments and recent satellite observations also show that an upstream wave may exist when the fluid Froude number is close to unity and the height of topography is in the right range.

AGW and AVS contribute to the spatial fluctuations of lower atmospheric wind and temperature fields over large ocean areas. On top of the marine atmospheric boundary layer, the wind field associated with an AVS or AGW causes the cloud structure to change around an obstacle, allowing the AVS or AGW to be observed in satellite visible and infrared images under conditions of high humidity, such as those sometimes found in maritime areas [*Hubert and Krueger, 1962; Chopra and Hubert, 1964, 1965; Tsuchiya, 1969; Thomson et al., 1977; Gjevik and Marthinsen, 1978; Mitchell, 1990; Li et al., 2001*]. At the bottom of the atmospheric boundary layer, the wind velocity fluctuation at the sea surface associated with an AVS or AGW modulates the sea surface roughness allowing imaging of these features by Synthetic Aperture Radar (SAR) through the resonant Bragg scattering mechanism. Such examples include atmospheric lee waves [*Vachon et al., 1994; Li et al., 1998, Zheng et al., 1998*], gravity waves [*Thomson et al., 1992; Chunchuzov et al., 2000*], atmospheric boundary layer rolls and atmospheric fronts [*Mourad, 1999*], mesoscale phenomena such as polar mesoscale cyclones and hurricanes [*Friedman and Li, 2000*], island wakes [*Pan and Smith, 1999*], cold air outbreaks [*Thompson et al., 1983*] and atmospheric vortex streets [*Li et al., 2000*].

The spatial coverage and resolution of satellite SAR imagery make it an excellent tool to study AVS and AGW whose spatial scale ranges from 100 km to 400 km. This scale is too small to be resolved by a synoptic observation network and too large to be observed by a single station, but can be readily captured in a single satellite SAR image.

In this chapter, we introduce recent AVS and AGW studies using RADARSAT-1 SAR images. Three cases of AVS using RADARSAT-1 ScanSAR Wide SAR images are presented. In addition, four examples of SAR observations of AGW are presented to demonstrate SAR's capability to measure associated near-surface wind field variations. AGW are presented in the form of both transverse and diverging lee waves and upstream propagating waves. From SAR images, radiosonde data, and surface weather charts, the typical parameters associated with AGW and AVS (i.e., AGW wavelength, the phase lines pattern, near surface wind field, as well as AVS lengths, vortex shedding period, shedding starting time, vortex tangential velocity and the energy dissipated during the vortex lifetime) can be derived.

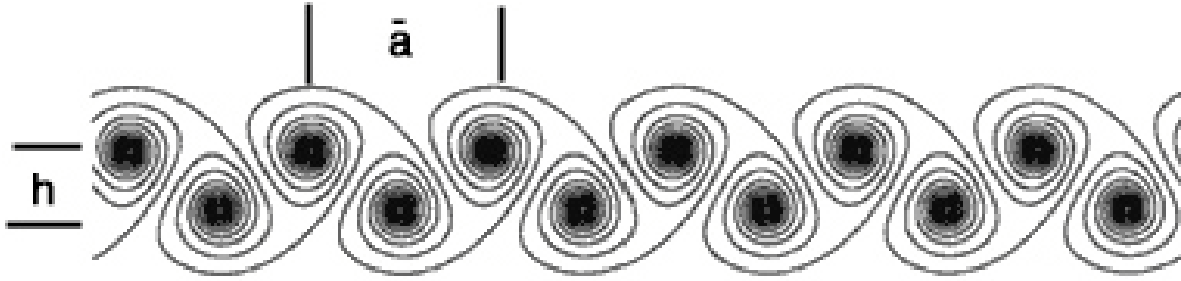


Figure 16.1. Schematic plot of a Kármán vortex street generated by wind passing a cylindrical obstacle of diameter D . a is the vortex wavelength, and h is the width of the Kármán vortex street.

16.2 Atmospheric Vortex Streets (AVS) Observed by SAR

The AVS pattern consists of counter rotating vortex-pairs shedding alternately near each edge of the obstacle and resembles the classic Von Kármán vortex-street patterns observed in laboratory flow experiments and illustrated in Figure 16.1. Although atmospheric vortex shedding from large islands was suggested as early as the 1930s, it was not until the early 1960s that researchers [e.g., *Hubert and Krueger*, 1962; *Chopra and Hubert*, 1964, 1965] observed the AVS pattern in the atmosphere in cloud images taken by the first generation of earth orbiting satellites.

The ratio h/a (see Figure 16.1) is a basic property of an AVS. Laboratory experiments show that a stable vortex formed on the lee side of an obstacle is characterized by $0.28 < h/a < 0.52$ [*Chopra and Hubert*, 1964; *Lugt*, 1983]. h/a for the Madeira Island [*Chopra and Hubert*, 1965] and Cheju Islands [*Tsuchiya*, 1969] case studies were 0.43 and 0.33, respectively. Five AVS patterns observed near the Aleutian Islands by *Thomson et al.* [1977] had h/a between 0.30 and 0.60.

The RADARSAT-1 SAR images (Figure 16.2 and 16.3) considered in this chapter are RADARSAT-1 ScanSAR Wide B mode images that were processed at the Alaska Satellite Facility as a QuickLook product (with spatial resolution of 200 m and pixel spacing of 100 m).

Table 16.1. h/a ratio for different case studies using remote sensing images

	Chopra and Hubert [1965]	Tsuchiya [1969]	Thomson et al. [1977]	Li et al.[2000]
h/a	0.43	0.33	0.30-0.60	0.4-0.45

The dimensions of the two AVS patterns in Figure 16.2 can be measured directly from the RADARSAT-1 SAR image. The h/a ratio for these two AVS's is between 0.40 and 0.45. We also observe that the h/a ratio varies for different AVS observed on the same SAR image. This is because the vortex shedding depends on the size and shape of the obstacle as well as the flow characteristics. Different obstacles from different islands also cause variation in h/a . In addition, this ratio becomes larger downstream during the decay of the vortices. Table 16.1 gives the observed h/a value by several researchers using remote sensing images.

The vortex shedding frequency, f , can be calculated from the vortex propagation velocity, U_e , and the vortex wavelength, a , as (U_e/a) . If consecutive satellite images showing the evolution of the same AVS are available, U_e can be estimated. In the two cases mentioned

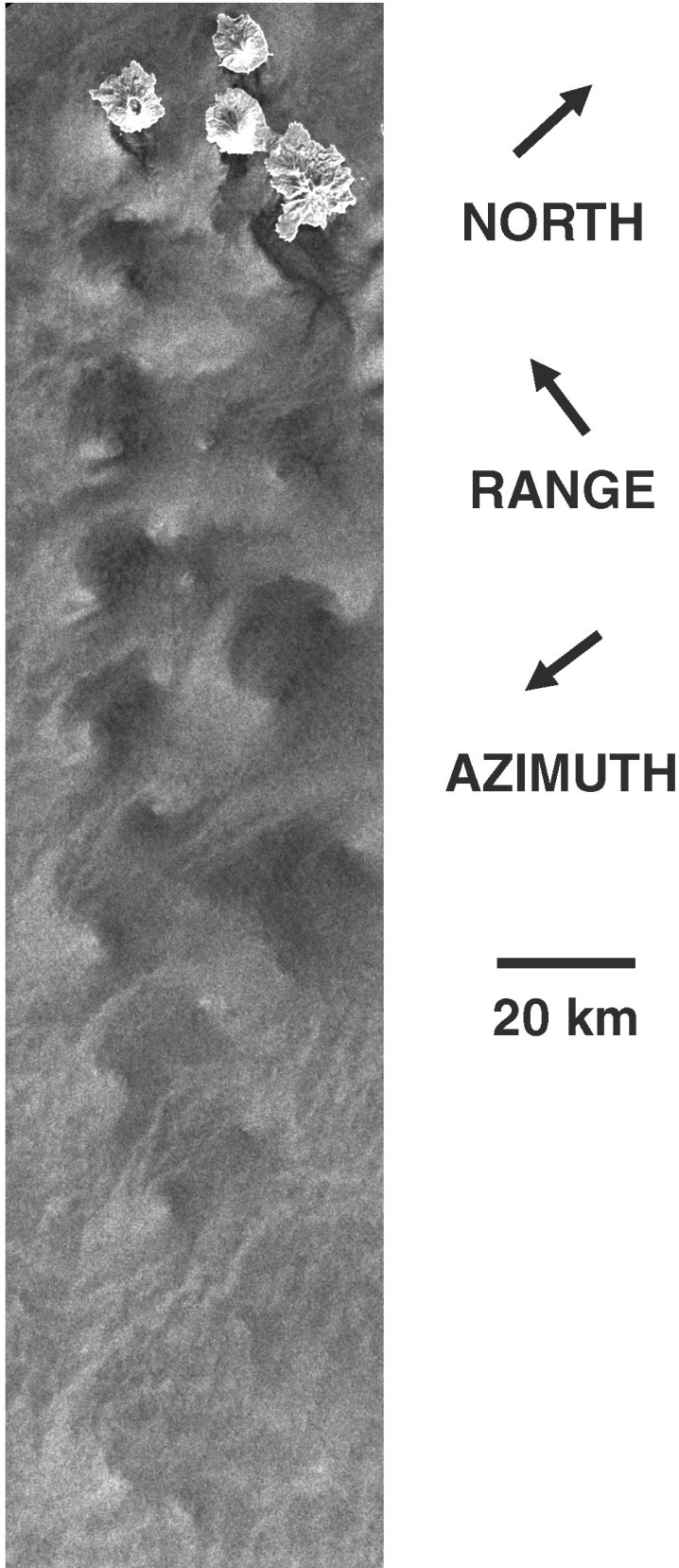


Figure 16.2. A RADARSAT-1 (C-band, HH) ScanSAR Wide B SAR subimage containing the sea surface imprint of two atmospheric vortex streets. The image center is located at roughly 52°N and 172°W, and covers the western side of the Gulf of Alaska. The image was acquired at 1725 UTC on 5 May 1999. ©CSA 1999

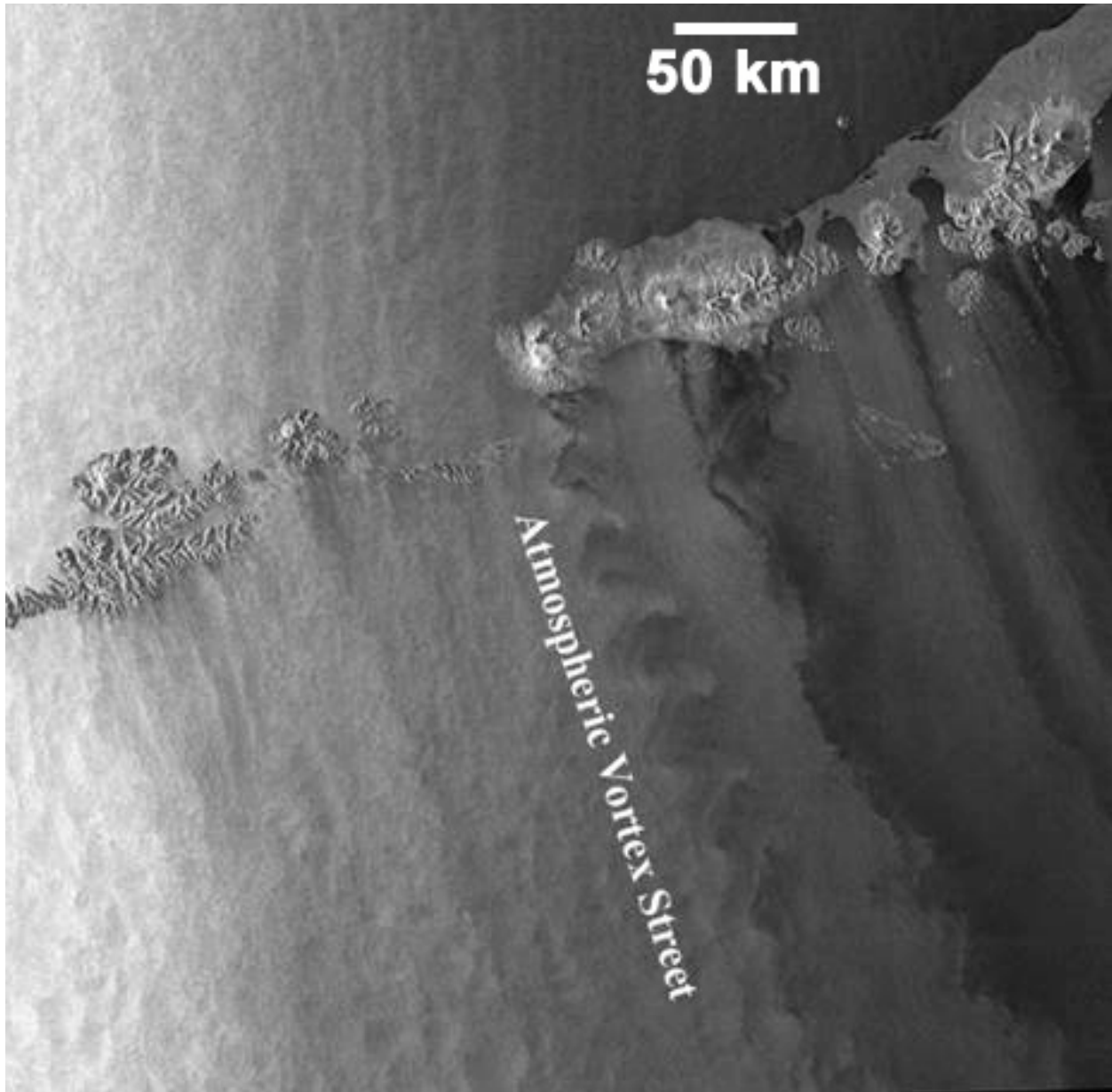


Figure 16.3. An example of Atmospheric Vortex Street observed by RADARSAT-1 (C-band, HH) SAR. Image was acquired 22 December 1999 at 0441 UTC. ©CSA 1999

above, only one SAR image is available, but one can still estimate U_e from U_o , the undisturbed wind velocity. The relationship between U_e and U_o is given as $U_e = 0.75U_o$ [Tsuchiya, 1969]. U_o can be obtained from radiosonde measurements. Measuring the length (L) of the AVS from the SAR images, one can calculate the vortex lifetime, $t = L/U_e$.

The tangential vortex velocity at the outer edge of the vortex, V_θ , is given by (1) [Wilkins, 1968; Li *et al.*, 2000]:

$$V_q = (k/2pR)[1 - e^{(-R^2/4ut)}] \quad (1)$$

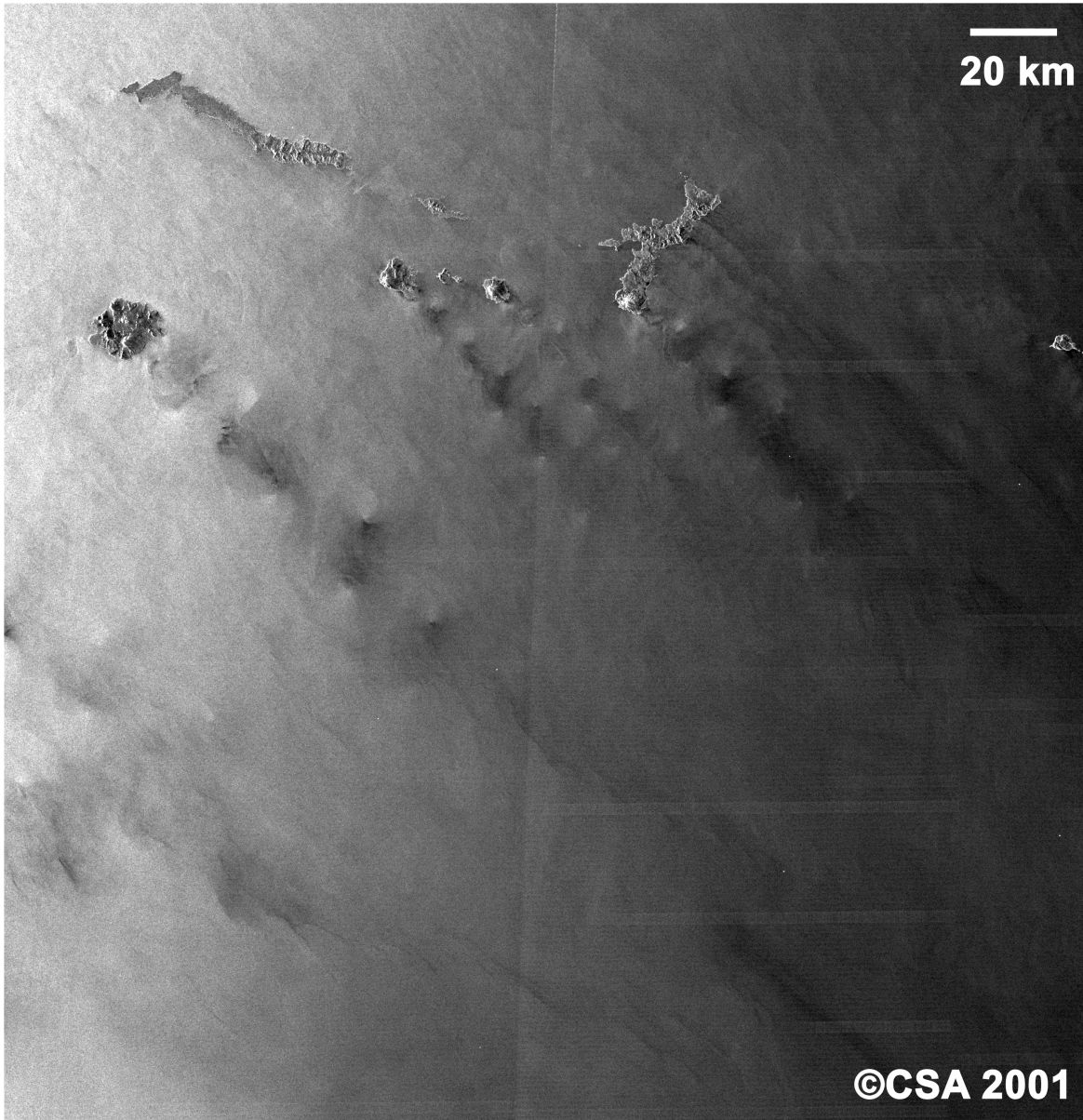


Figure 16.4. RADARSAT-1 (C-band, HH) ScanSAR Wide image showing six Atmospheric Vortex Streets developed at the lee of Aleutian Island. The image was acquired on 22 March 2001 at 1827 UTC. ©CSA 2001

where k is the circulation strength, t is time, n is the eddy viscosity, and R is the radius of each vortex. The total energy dissipated by a vortex during its lifetime is given by (2) [Wilkins, 1968]:

$$\frac{1}{\rho_0} \int_{t_0}^t \epsilon dt = \frac{1}{\rho_0} (k^2 / 16 \pi^2 \rho_0) \left[1 + \sum_{n=1}^{\infty} \frac{(-R/2ut_0)^n}{(n+1) \cdot (n+1)!} \right] \quad (2)$$

where ρ_0 is the air density (1 kg m^{-3}), ϵ is the rate of vortex energy dissipation, n is the eddy viscosity, t_0 is the starting time and should be small compared to the vortex's life time, t .

In the case represented in Figure 16.2, the wind velocity measured by radiosonde from a nearby meteorological station reveals that the wind velocity at the atmospheric inversion layer is about 15.9 m s^{-1} . From SAR image (Figure 16.2), we measure that the length of the two AVS are 196 km and 111 km, respectively. Using these equations, we estimate that vortex lifetime, t , is between 2.5 to 5 hr, and shedding period is between 0.5 and 1 hr.

In the two AVS cases demonstrated in Figure 16.2, the vortex diameter is measured to be about 4 km. Therefore, we estimate that the tangential vortex velocity, V_q , is between 1.6 m s^{-1} and 2.3 m s^{-1} . The total energy dissipation for the oldest AVS vortices is 25 J m^{-3} . These values are about 50 percent smaller than those estimated by *Wilkins* [1968], presumably because the sizes and strength of the vortices in this case are much smaller.

Figures 16.3 and 16.4 show several AVS's observed in RADARSAT-1 ScanSAR Wide SAR images. In both cases, the surface pressure maps and radiosonde measurements reveal that low pressure dominates the observational area. In Figure 16.3, the AVS contains 10 vortex-pairs extending over 200 km. One of the advantages of RADARSAT-1 ScanSAR is that it can cover up to a 525 km swath, which is five times wider than the ERS-1/2 SAR. The ScanSAR Wide SAR image in Figure 16.4 covers a wide range of the Aleutian Islands between 179°W and 186°W . There are five AVSs shedding from five different islands in this image. Under similar atmospheric conditions, the width of AVS and the radius of the vortex within each AVS are quite different because of island size and height differences.

16.3 Atmospheric Gravity Waves (AGW) Observed by SAR

16.3.1 Island lee waves

Atmospheric gravity waves (AGW) generated by flow over a topographical features can exist downstream and upstream of the feature, depending upon the atmospheric Froude number, stratification, and topographic forcing [*Baines*, 1995]. The downstream waves are often standing waves, called lee waves [*Gossard and Hooke*, 1975]. As long as the atmospheric stratification and wind profile remain constant, their wave crest and trough remain the same. In order to remain a standing wave, the lee wave phase velocity must be equal in magnitude and opposite in direction to the airstream.

Wavelengths of AGW range from a few to several tens of kilometers [*Thomson et al.*, 1992; *Vachon et al.*, 1994; *Li et al.* 1998; *Zheng et al.* 1998; *Mourad*, 1999; *Chunchuzov et al.* 2000]. These waves arise from the action of buoyancy forces on air particles displaced from their equilibrium state in a stably stratified atmosphere. AGW can carry aircraft upward or downward, sometimes causing serious safety problems [*Christine*, 1983]. AGW are usually observed as wave-like patterns in SAR images, in the form of: (1) the transverse wave type where the wave crests are nearly perpendicular to the wind direction; and (2) the diverging wave type where the wave crests are orientated outwards from the center of the wake. In the diverging wave case, the wave crests are located within a wedge-shaped wake behind the terrain obstacle. The AGW crest patterns which can occur behind an island are illustrated in Figure 16.5.

Due to the fine spatial resolution of the RADARSAT-1 SAR (100 m resolution for the ScanSAR 500 km wide swath), a periodic variation in radar backscatter signal intensity caused by AGW may easily be seen in RADARSAT-1 images. The SAR images show the detailed form of the lee wave patterns and allow us to estimate various characteristic parameters such as wavelength, amplitude, and the angle of the wedge for diverging lee waves. Figure 16.6 is an example of a group of transverse lee waves observed in RADARSAT-1 ScanSAR Wide B mode

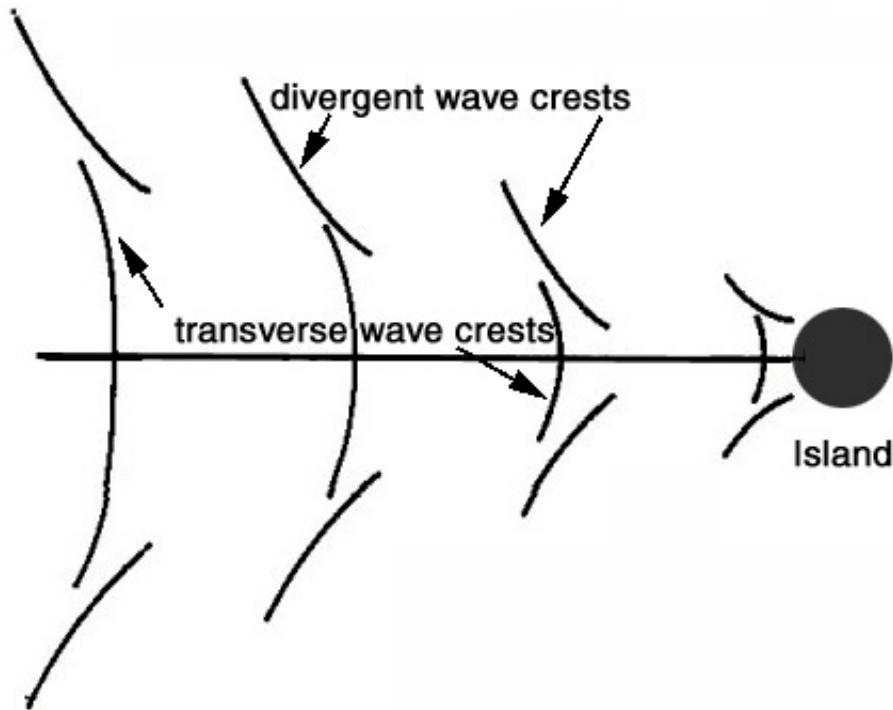


Figure 16.5. Schematic plot of atmospheric gravity wave crests pattern behind an island.

SAR image. Figure 16.7 shows the diverging lee wave pattern. Figure 16.8 is a 3-D view of a transverse lee wave pattern. The wave parameters depend strongly on the wind speed and temperature stratification of the airflow. Therefore, the availability of atmospheric sounding data that can provide the atmospheric stratification close to the imaged area is of great importance in the interpretation of the observed wave patterns.

AGWs observed in SAR images (Figures 16.6 through 16.8) often cover large ocean areas and appear in the images as wave trains with certain wavelengths. This shows that we are likely dealing with trapped internal wave modes propagating horizontally in atmospheric waveducts. The waveducts are often formed in the stable layers of the lower atmosphere with high local values of buoyancy frequency and act as filters for the frequencies of the trapped internal waves.

Lee wave models have been used to simulate atmospheric lee wave characteristics. One-dimensional [Vachon *et al.*, 1994] and two-dimensional [Chunchuzov *et al.*, 2000] lee wave models have been used to study both transverse and diverging lee waves observed on European Remote Sensing Satellite (ERS-1) SAR and RADARSAT-1 SAR images. Both studies show reasonable agreement between the SAR observed AGW characteristics and the model-simulated wave parameters.

Atmospheric boundary layer rolls are also commonly observed in SAR images as linear streaks [Alpers and Brummer, 1994; Brown, 2000; Levy, 2001]. These streaks are caused by the convergence/divergence of atmospheric boundary layer rolls in the planetary boundary layer [Brown, 2000]. There are some differences between atmospheric boundary layer rolls and lee waves. First, ocean surface imprints of atmospheric boundary layer rolls are nearly parallel to the surface wind direction, but lee waves streaks are usually perpendicular to the wind direction; second, the spatial scale of atmospheric boundary layer rolls is usually smaller than that of lee

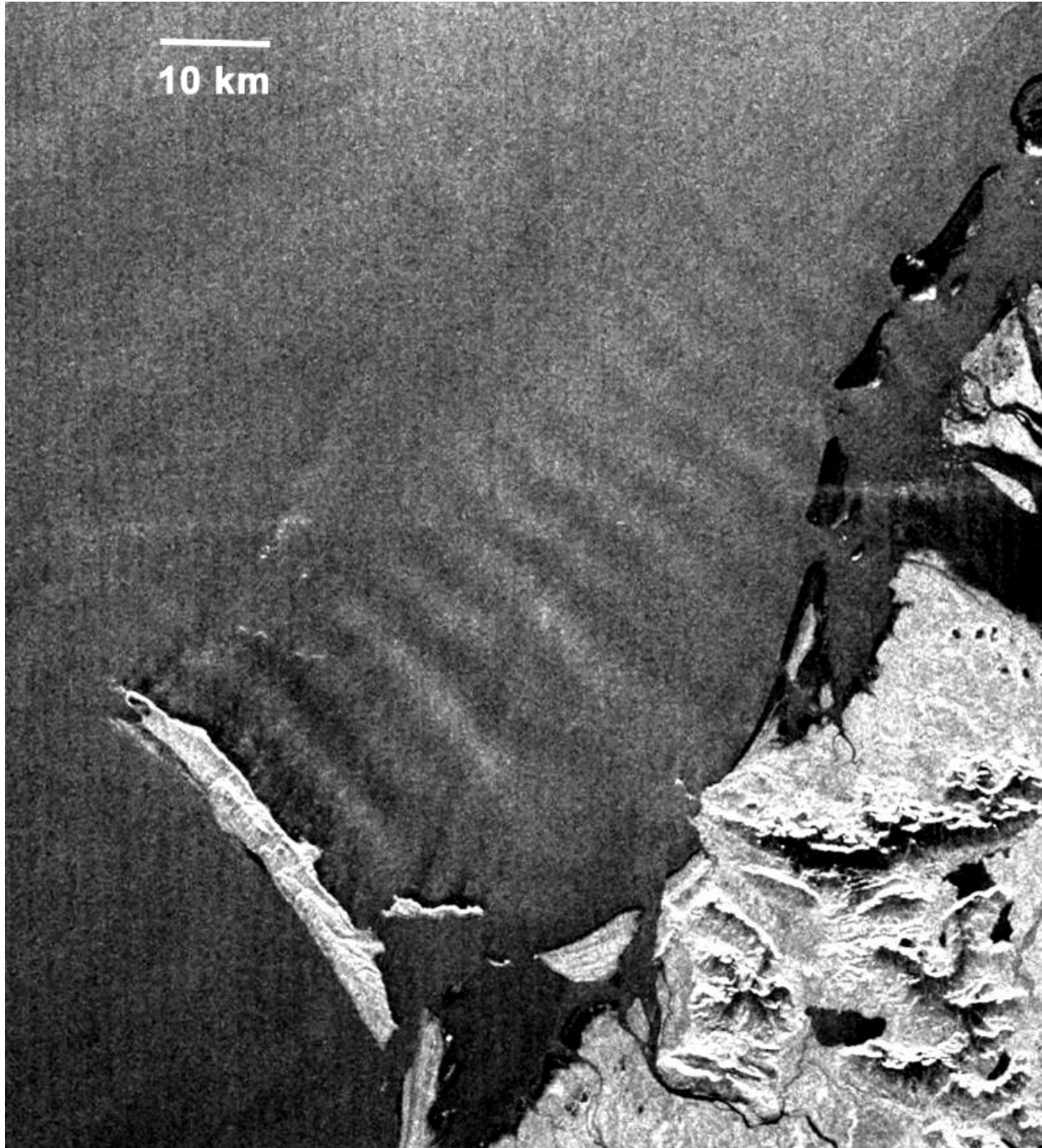


Figure 16.6. A RADARSAT-1 (C-band, HH) ScanSAR Wide B SAR subimage containing the sea surface imprint of transverse atmospheric gravity waves. The image center is at 60°N, 145°W. The image was acquired 12 June 2001 at 0310 UTC. ©CSA 2001

waves; third, lee waves are associated with topography features, where atmospheric boundary layer rolls can happen without this limitation. Therefore, if the coincident wind measurements from radiosonde are available when a SAR image is acquired, one can distinguish the two phenomena from the alignment of wind direction and the direction of the linear streak in the SAR image.

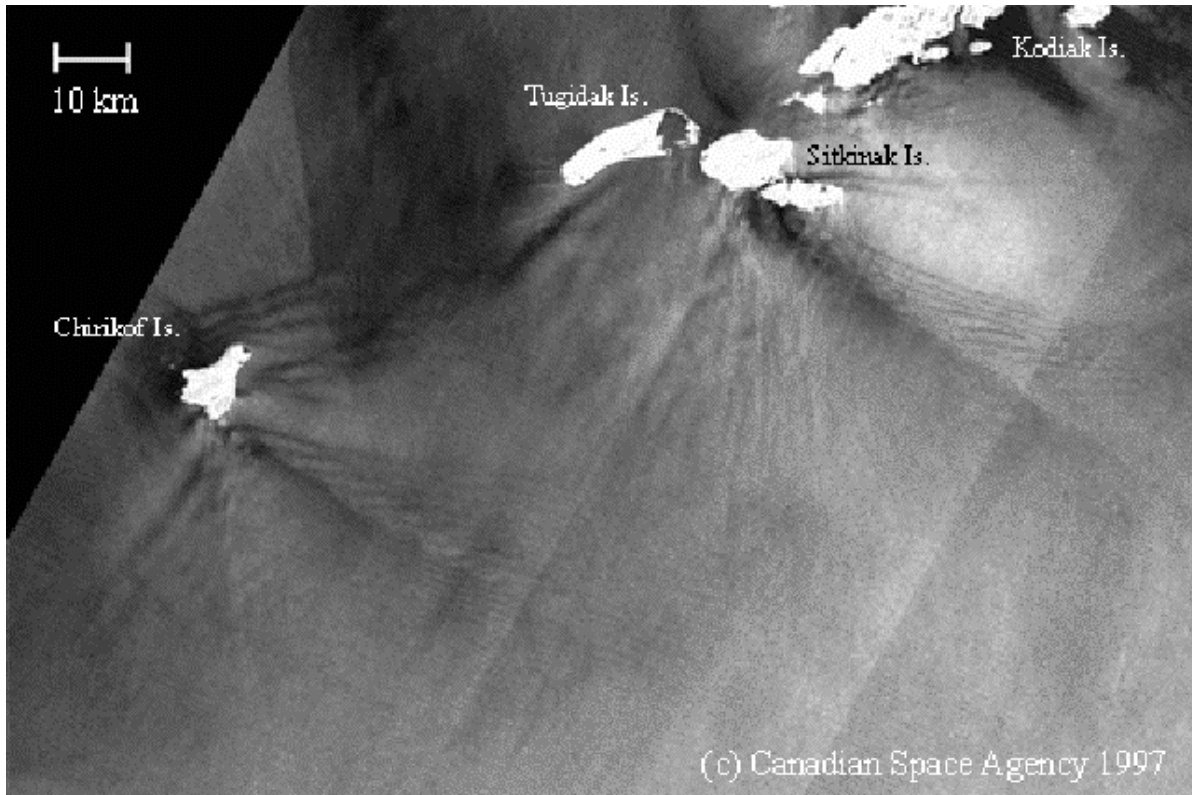


Figure 16.7. RADARSAT-1 (C-band, HH) ScanSAR Wide image shows diverging island lee wave pattern in the Gulf of Alaska. The image center is at 55°N, 154°W. The SAR image was acquired 27 June 1997 at 1629 UTC.

16.3.2 Upstream waves

AGW may also propagate in the upstream direction. The upstream wave characteristics can be explained by linear wave equations as well as classic Korteweg-de Vries (KdV), or extended KdV (eKdV) [Miles, 1979] or forced extended KdV (feKdV) [Melville and Helfrich, 1987] equations. Theoretical considerations of this phenomenon have been described for one layer systems (fKdV) [Akylas, 1984; Wu, 1987] and two-layer systems (feKdV) [Melville and Helfrich, 1987]. The non-dimensional governing equation for the feKdV equation is in the form of:

$$\mathbf{h}_t + (U - C_o)\mathbf{h}_x - \frac{3C_o}{2d_o}\mathbf{h}\mathbf{h}_x - \frac{1}{6}C_o d_o^2 \mathbf{h}_{xxx} = \frac{1}{2}U\mathbf{h}_x \quad (3)$$

where η is the interface displacement, U is the mean airflow velocity, C_o is the wave phase velocity, and h is the characteristic height of the local topography, h_x represents the topography forcing in the horizontal (X-axis) direction. The upstream waves happen when the Froude number (f) is close to unity, and they depend upon the characteristic height of the local topography (h). The f - h diagram in the neighborhood of $\langle f = 1 \rangle$ shows the different characters of the solution to the feKdV equation [Grimshaw and Smyth, 1986]. The dark-bright upstream AGW pattern in Figure 16.9 is similar to the lee wave patterns in Figure 16.6 and 16.8. However, in this case, the surface map and local radiosonde measurement show that the wave packet is propagating against the airflow.

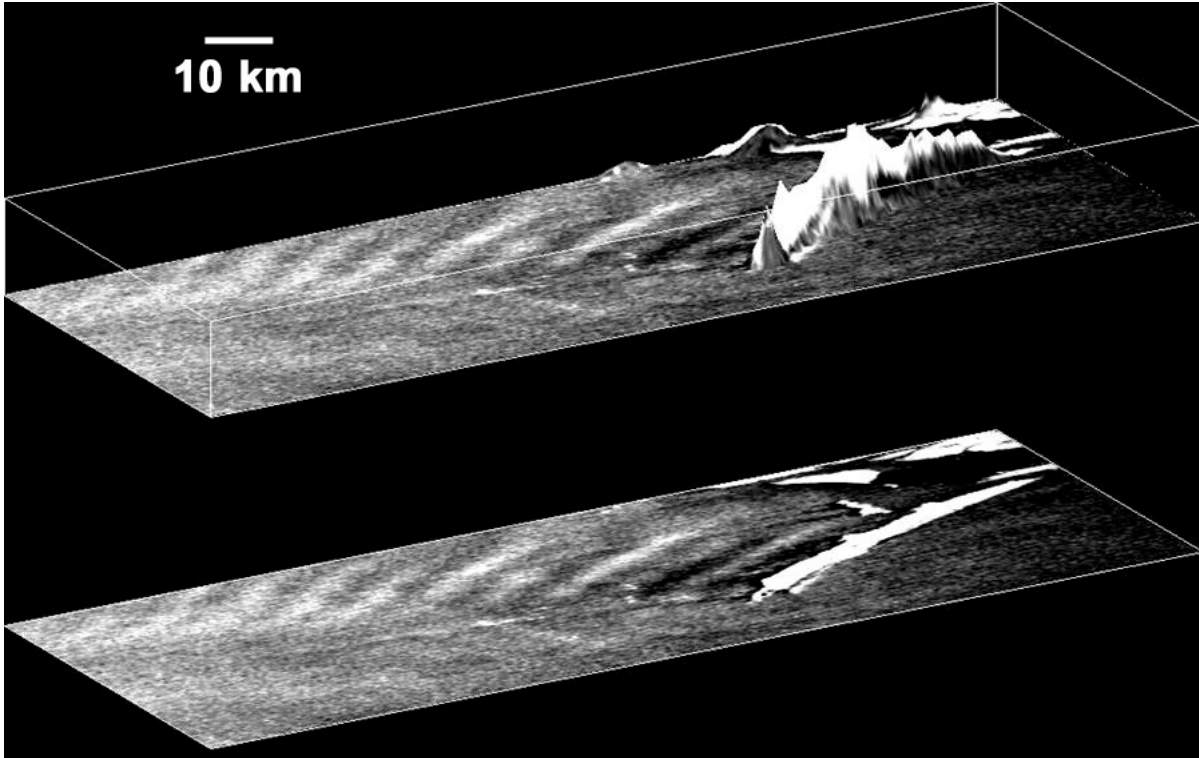


Figure 16.8. A RADARSAT-1 (C-band, HH) ScanSAR Wide B SAR subimage containing the sea surface imprint of upstream propagating topographic waves. The SAR image is draped on the local terrain map. The image was acquired 6 June 2001. ©CSA 2001

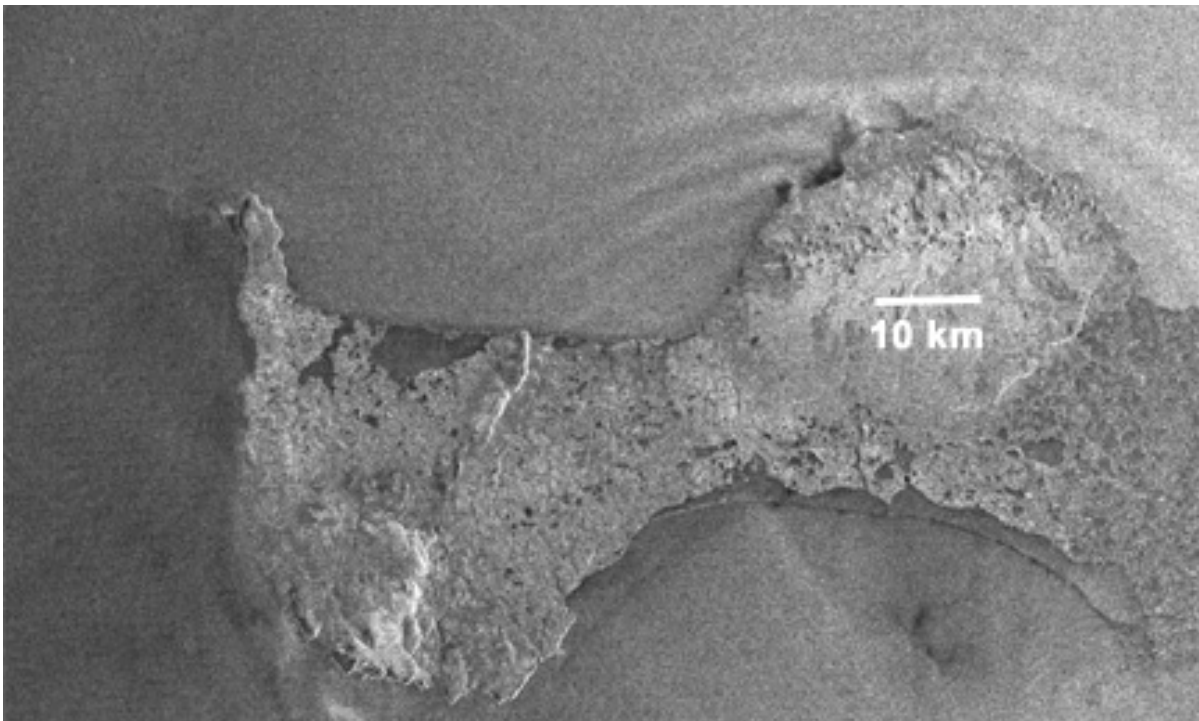


Figure 16.9. A RADARSAT-1 (C-band, HH) ScanSAR Wide B SAR subimage containing the sea surface imprint of upstream propagating topographic waves north of St. Lawrence Island in the Bering Sea. The image was acquired at 7 September 1997. ©CSA 1997

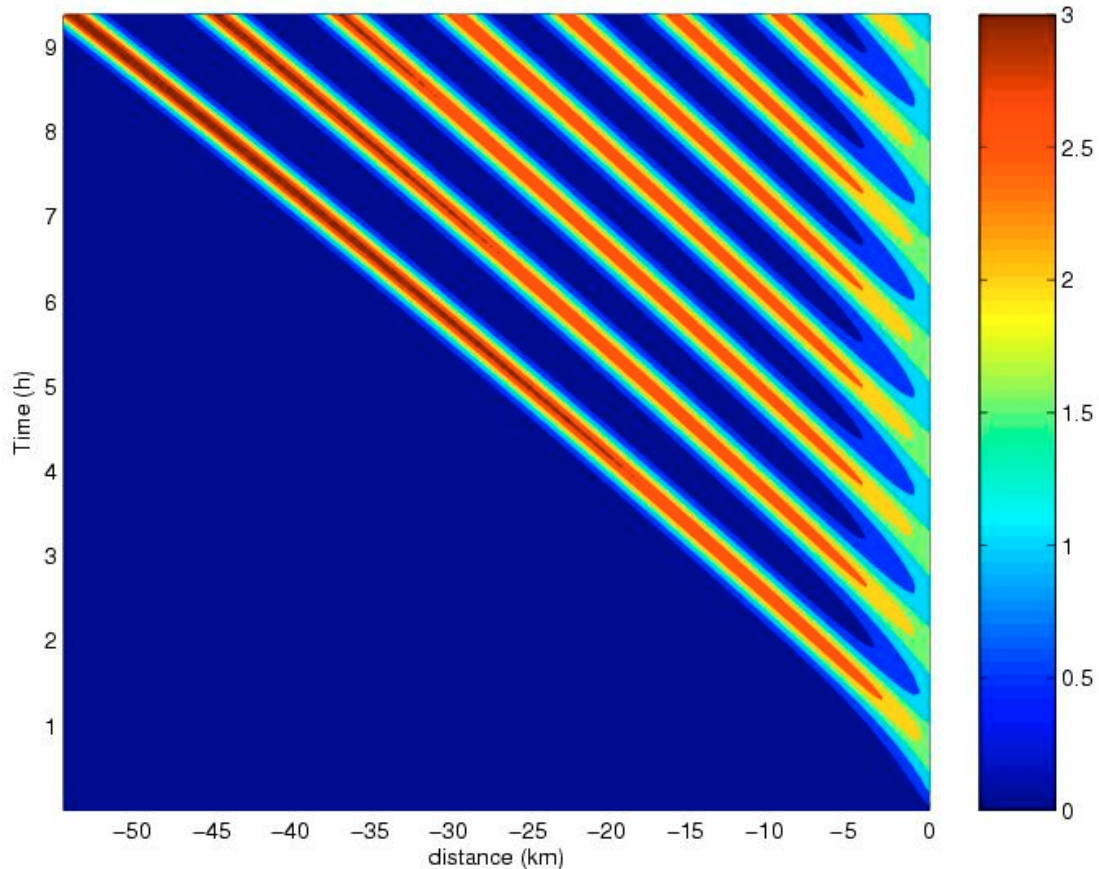


Figure 16.10. Wave evolution is simulated by numerically solving the two-layer fKdV at Froude number $F = 0.95$. In this figure the wave propagation is demonstrated in dimensional x - t space. The color scale represents the non-dimensional interface displacement.

Solutions of Eq. (3) can be obtained numerically using the explicit finite-difference scheme of *Vliegenthart* [1971]. In numerical experiments, we specify the values of parameters in Eq. (3) based on radiosonde measurements at the SAR image taken time and St. Lawrence Island dimensions. Figure 16.10 displays the evolution of the upstream solitons in the dimensional time-space (t - x) at Froude number $F = 0.95$. [*Li et al.* 2004].

16.3.3 Coastal frontal waves

Another type of AGW often observed near coastlines is called a coastal frontal wave. This type of AGW is not generated by the local topography, but by the land-sea temperature difference and the coastal circulation regime. Coastal frontal waves have been observed on an ERS-1 SAR image off Taiwan Strait [*Zheng et al.*, 1998] and on images of Advanced Very High Resolution Radiometer data from the NOAA polar orbiting satellites taken along the Texas coast [*Li et al.*, 2001]. The sea surface imprints and the cloud structure modulations from these waves are the same as those of mountain or island lee waves. The waves are generally parallel to the coastline with wavelength about 10 km. The wave crest line can extend for more than 500 km. The wave can be simulated using the coastal frontal wave model [*Zheng et al.*, 1998; *Li et al.*, 2001].

16.4 Conclusion

In summary, SAR images can provide detailed information on spatial wind field variations associated with AGWs and AVSs over large ocean areas. The shape and scale of the AGWs produced by islands can be explained using a flow over topography model. The most commonly observed waves are mountain or island lee waves. However, when the Froude number is close to unity, the wave may propagate against the airflow in the upstream direction. In this chapter, several AGW examples observed by RADARSAT-1 SAR are given, and the general characteristics and scales of these waves are discussed. The SAR images, along with sounding data available from nearby stations, can allow us to identify the generation mechanisms, and thus choose the right model to further study these waves. With more observations made from other satellites sensors, i.e., Moderate Resolution Imaging Spectroradiometer (MODIS), Sea-viewing Wide Field-of-view Sensor (SeaWiifs) and NOAA Advanced Very High Resolution Radiometer (AVHRR), we may, in the near future, observe the temporal evolution of the waves and then validate the model calculated wave temporal variation.

The SAR-observed atmosphere vortex streets can be interpreted as the atmospheric analog of classic Von Kármán vortex streets. The length and the ratio of the width of the Von Kármán vortex street (h) and the vortex spacing (a) can be measured from SAR images. On the basis of this SAR image and a nearby radiosonde observations, the vortex shedding period, tangential velocity at the outer edge of the vortex, the vortex lifetime, and the total energy dissipation can be estimated using the Von Kármán vortex streets theory.

16.5 References

- Alpers, W., and B. Brummer, 1994: Atmospheric boundary layer rolls observed by the synthetic aperture radar aboard the ERS-1 satellite. *J. Geophys. Res.*, **99**, 12 613–12 621.
- Akylas, T. R., 1984: On the excitation of long nonlinear water waves by a moving pressure distribution. *J. Fluid Mech.*, **141**, 455–466.
- Baines, P. G., 1995: *Topographic Effects in the Stratified Flows*. Cambridge University Press, 498 pp.
- Birkhoff, G., and E. H. Zarantonello, 1957: *Jets, Wakes and Cavities*. Academic Press, 353 pp.
- Brown, R. A., 2000: Serendipity in the use of satellite scatterometer, SAR and other sensor data. *Johns Hopkins APL Tech. Dig.*, **21**, 21–26.
- Chopra, K. P., and L. F. Hubert, 1964: Kármán vortex streets in earth's atmosphere. *Nature*, **203**, 1341–1343.
- , and ———, 1965: Mesoscale eddies in wake of islands. *J. Atmos. Sci.*, **22**, 652–657.
- Chunchuzov, I., P. Vachon, and X. Li, 2000: Analysis and modeling of atmospheric gravity waves observed in RADARSAT SAR images. *Remote Sens. Environ.*, **74**, 343–361.
- Christine, D. R., 1983: Solitary waves as aviation hazard, *EOS*, **64**, 67.
- Etling, D., 1989: On atmospheric vortex streets in the wake of large islands. *Meteor. Atmos. Phys.*, **41**, 157–164.
- , 1990: Mesoscale vortex shedding from large islands: A comparison with laboratory experiment of rotating stratified flows. *Meteor. Atmos. Phys.*, **43**, 145–151.
- Friedman, K. S., and X. Li, 2000: Monitoring hurricanes over the ocean with wide swath SAR. *Johns Hopkins APL Tech. Dig.*, **21**, 80–85.
- Gjevik, B., and T. Marthinsen, 1978: Three-dimensional lee-wave pattern. *Quart. J. Roy. Meteor. Soc.*, **104**, 947–957.

- Gossard, E. E., and W. H. Hooke, 1975: *Waves in the Atmosphere*. Elsevier Scientific Publishing, 456 pp.
- Grimshaw, R. H. J., and N. Symth, 1986: Resonant flow of a stratified fluid over topography. *J. Fluid Mech.*, **169**, 429–464.
- Hubert, L. F., and A. F. Krueger, 1962: Satellite pictures of mesoscale eddies. *Mon. Wea. Rev.*, **90**, 457–463.
- Levy, G., 2001: Boundary layer roll statistics. *Geophys. Res. Lett.*, **28**, 1993–1995.
- Li, X., W. Pichel, K. Friedman, and P. Clemente-Colón, 1998: The sea surface imprint of island lee waves as observed by RADARSAT synthetic aperture radar. *Proc. 1998 Int. Geoscience and Remote Sensing Symp.*, Seattle, WA, IEEE, 763–766.
- , P. Clemente-Colón, W. Pichel and P. Vachon, 2000: Atmospheric vortex streets on a RADARSAT SAR image. *Geophys. Res. Lett.*, **27**, 1655–1658.
- , Q. Zheng, W. Pichel, X. Yan, W. Liu, P. Clemente-Colón, 2001: Analysis of coastal lee waves along the coast of Texas observed on AVHRR images. *J. Geophys. Res.*, **106**, 7017–7025.
- , C. Dong, P. Clemente-Colón, W. G. Pichel, and K. S. Friedman, 2004: Synthetic aperture radar observation of the sea surface imprints of upstream atmospheric solitons generated by flow impeded by an island, *J. Geophys. Res.*, **109**, C02016, doi:10.1029/2003JC002168.
- Lugt, H. J., 1983: *Vortex Flow in Nature and Technology*. John Wiley & Sons, 297 pp.
- Melville, W. K., and K. R. Helfrich, 1987: Transcritical two-layer flow over topography. *J. Fluid Mech.*, **178**, 31–52.
- Miles, J. W., 1979: On internal solitary waves. *Tellus*, **31**, 456–462.
- Mitchell, R. M., R. P. Cechet, P. J. Turner, and C. C. Elsum, 1990: Observation and interpretation of wave clouds over Macquarie Island. *Quart. J. Roy. Meteor. Soc.*, **116**, 741–752.
- Marthinsen, T., 1980: Three-dimensional lee waves. *Quart. J. Roy. Meteor. Soc.*, **106**, 569–580.
- Mourad, P. D., 1999: Footprints of atmospheric phenomena in synthetic aperture radar images of the ocean surface—A review. *Air-sea fluxes—Physics, chemistry, and dynamics*, G. Geernaert, Ed., Kluwer Academic Publishers, 640 pp.
- Smith, R. B., and V. Grubisic, 1993: Aerial observation of Hawaii’s wake. *J. Atmos. Sci.*, **50**, 3728–3750.
- , and D. F. Smith, 1995: Pseudoinviscid wake formation by mountains in shallow-water flow with a drifting vortex. *J. Atmos. Sci.*, **52**, 436–454.
- , A. C. Gleason, P. A. Gluhosky, and V. Grubisic, 1997: The wake of St. Vincent. *J. Atmos. Sci.*, **54**, 606–623.
- Thomson, R. E., J. F. R. Gower and N. W. Bowker, 1977: Vortex streets in the wake of the Aleutian Islands. *Mon. Wea. Rev.*, **105**, 873–884.
- , P. W. Vachon, and G. A. Borstad, 1992: Airborne synthetic aperture radar imagery of atmospheric waves. *J. Geophys. Res.*, **97**, 14 249–14 257.
- Tsuchiya, K., 1969: The clouds with the shape of Kármán vortex street in the wake of Cheju Island, Korea. *J. Meteor. Soc. Japan*, **47**, 457–464.
- Vachon, P., O. Johannessen, and J. Johannessen, 1994: An ERS-1 synthetic aperture radar image of atmospheric lee waves. *J. Geophys. Res.*, **99**, 22 843–22 490.
- Vliedhart, A. C., 1971: On finite-difference methods for the Korteweg-de Vries equation, *J. Eng. Maths.*, **5**, 137-155

- Wilkins, E. M., 1968: Energy dissipated by atmospheric eddies in the wake of islands. *J. Geophys. Res.*, **73**, 1877–1881.
- Wu, T. Y., 1987: Generation of upstream advancing solitons by moving disturbances. *J. Fluid Mech.*, **184**, 75–99.
- Zheng, Q., X.-H. Yan, V. Klemas, C.-R. Ho, N.-J. Kuo, and Z. Wang, 1998: Coastal lee waves on ERS-1 SAR images. *J. Geophys. Res.*, **103**, 7979–7993.